



LAWRENCE
LIVERMORE
NATIONAL
LABORATORY

IEEE Trans. Plas. Sci. paper - First Experiments and Radiographs on the MegaJOuLe Neutron Imaging Radiography (MJOLNIR) Dense Plasma Focus

D. Offermann, D. Welch, D. Rose, C. Thoma, R. Clark, C. Mostrom, A. Schmidt, A. Link

October 8, 2021

IEEE Transactions of Plasma Science

Disclaimer

This document was prepared as an account of work sponsored by an agency of the United States government. Neither the United States government nor Lawrence Livermore National Security, LLC, nor any of their employees makes any warranty, expressed or implied, or assumes any legal liability or responsibility for the accuracy, completeness, or usefulness of any information, apparatus, product, or process disclosed, or represents that its use would not infringe privately owned rights. Reference herein to any specific commercial product, process, or service by trade name, trademark, manufacturer, or otherwise does not necessarily constitute or imply its endorsement, recommendation, or favoring by the United States government or Lawrence Livermore National Security, LLC. The views and opinions of authors expressed herein do not necessarily state or reflect those of the United States government or Lawrence Livermore National Security, LLC, and shall not be used for advertising or product endorsement purposes.

First Experiments and Radiographs on the MegaJoule Neutron Imaging Radiography (MJOLNIR) Dense Plasma Focus

A. Schmidt, *Member, IEEE*, E. Anaya, M. Anderson, *Member, IEEE*, J. Angus, S. Chapman, C. Cooper, O. Drury, C. Goyon, S. Hawkins, D. P. Higginson, I. Holod, E. Koh, A. Link, *Member, IEEE*, D. Max, M. McMahon, J. Mitrani, Y. Podpaly, *Member, IEEE*, A. Povilus, and D. Van Lue

Abstract— A dense plasma focus (DPF) is a relatively compact coaxial plasma gun which completes its discharge as a Z-pinch. These devices are designed to operate at a variety of scales to produce short (<100 ns) pulses of ions, X-rays, and/or neutrons. LLNL recently constructed and brought into operation a new device, the MJOLNIR (MegaJoule Neutron Imaging Radiography) DPF, which is designed for radiography and high-yield operations. This device has been commissioned and has achieved neutron yields of up to $3.8E11$ neutrons/pulse at 2.5 MA peak current while operating at up to 1 MJ of stored energy in its original pulsed power configuration. MJOLNIR is equipped with a wide range of diagnostics, including nuclear activation detectors, neutron time-of-flight detectors, a fast-framing camera, optical light gates, and a time-gated neutron and x-ray imager. LLNL also runs unique particle-in-cell (PIC) simulations of DPF discharges in the Chicago code, and has gained significant insight into the various physical factors that influence neutron yield. MJOLNIR is one of the first DPFs whose design and continual upgrades are heavily influenced by model predictions. In this paper, we describe insights from modeling, device operation, and recent results. Comparisons between modeling predictions and measurements, as well as x-ray and neutron images are presented.

Index Terms—dense plasma focus, nuclear imaging, neutron sources, neutrons, plasma devices, plasma diagnostics, plasma pinches, plasma simulation, pulse power systems, radiography, z-pinch

I. INTRODUCTION

THE dense plasma focus (DPF) [1] is a coaxial plasma rail gun whose plasma discharge ends in a Z-pinch configuration. At the beginning of the discharge, the gas fill flashes over across the insulator, creating a conducting plasma sheath. Then the plasma sheath is accelerated down the length of the gun and then inward towards the axis by a self-generated magnetic field. Finally, the plasma current sheath pinches on axis, and eventually breaks up due to instabilities, dramatically increasing the plasma impedance leading to a large electric field across the plasma “target.” When operated with a deuterium or deuterium-tritium (DT) gas fill, a DPF produces a short pulse

(typically <100 ns) of neutrons through energetic ion collisions. DPFs can be scaled from several kA of plasma current to several MA of plasma current, with neutron production generally increasing as plasma current increases.

The MegaJoule Neutron Imaging Radiography (MJOLNIR) DPF (Fig. 1) was designed and built at Lawrence Livermore National Laboratory (LLNL) for the purpose of developing a viable neutron source for flash neutron radiography. MJOLNIR generated first plasmas on August 30, 2018, and first neutrons the following day. The electrodes on MJOLNIR were designed with the aid of hundreds of particle-in-cell simulations [2-5] of the plasma discharge. We present results from the first pulsed power configuration of MJOLNIR, (with up to 1 MJ of stored energy and up to 2.5 MA of plasma current), novel diagnostic results, and insights gained from the simulations.



Fig. 1. MJOLNIR DPF in 1 MJ stored energy configuration.

Submitted for publication on April 30, 2021. Prepared by LLNL under Contract DE-AC52-07NA27344.

A. Schmidt is staff at Lawrence Livermore National Laboratory (LLNL) in Livermore, CA, 94550 USA (email: schmidt36@llnl.gov). D. Max is affiliated

with the National Nuclear Security Site. Remaining authors were affiliated with LLNL at the time work was performed.

II. BACKGROUND

While results from numerous DPFs have been reported in the literature, only a select few are MA-class. DPFs with 2-3 MA of plasma current are pushing the limit of possible DPF performance, as higher-current DPF experiments have empirically shown to top out on neutron yield above a certain current.

Notable MA-class DPFs of the past include PF-1000 [6], SPEED 2 [7], and Poseidon [8]. MA-class DPFs operational today include Gemini at NNSS [9] and a DPF operated by a private company, Verus Research [10]. In the published literature, these DPFs report yields ranging from 1.2×10^{11} to 2.8×10^{11} neutrons per pulse when operated with deuterium.

III. METHODS AND MATERIALS

A. MJOLNIR

The 1-MJ configuration of the MJOLNIR pulsed power driver (Fig. 2) is composed of three 4.9 m-tall air-pressure-insulated Marx towers that house twelve single-stage Marx modules. Each Marx module consists primarily of two 34 μ F capacitors and a single high-current railgap switch, both from the decommissioned Atlas experiment [11-13]. The Marx towers generate a voltage and current pulse which is transferred via 84 flexible transmission line cables to a disk-like collector plate and ultimately through the coaxial DPF head and dynamic plasma load reaching 2.5 MA when the system is charged to ± 50 kV (i.e. 100 kV erected). Current waveforms from a discharge in which the anode and cathode are shorted with a conductor indicates that the bank (with voltage-reversal protection resistors), cables, and transmission plate have a lumped circuit capacitance of 204 μ F, inductance of 67.4 nH and resistance of 12.5 mOhm.



Fig. 2. Three of MJOLNIR's Marx bank "towers," containing 1 MJ stored energy at maximum voltage (100 kV).

The MJOLNIR electrodes are made of oxygen-free copper. The fielded anodes (Fig. 3) are 15.2 cm (6 inches) in diameter with exposed lengths varying from 18.3 to 22.1 cm depending on the anode. The anodes have pre-drilled hollows of radius 0.9 or 3.8 cm. The anode-cathode gap is fixed at 4.3 cm. The

plasma-facing insulator is made of the machinable ceramic MACOR® and has an exposed length of 4.6 cm. The MACOR® insulator mates to a PEEK or Ultem® base which are not directly exposed to plasma.

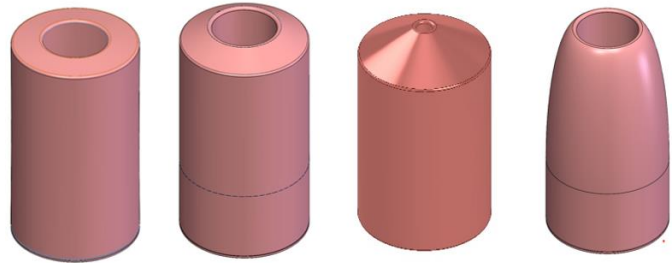


Fig. 3. MJOLNIR anodes fielded in 1 MJ pulsed power configuration. From left to right the anode models are referred to as A10-3.8-A, A30-3.8-A, A30-0.9-A, and P1-3.8-A. The anode names reference the degree of taper, if applicable, and the radius of the hollow in centimeters.

B. Diagnostics

MJOLNIR is outfitted with many diagnostics including a beryllium activation foil neutron detector, LaBr activation neutron detectors, scintillator/PMT neutron time-of-flight (nToF) diagnostics, a 16-frame Specialized Imaging fast visible light camera, "optical light gates"/photodiodes focused on the anode, a residual gas analyzer, and a Rogowski coil current measurement between the transmission plate and the DPF electrodes.

The Be activation foil diagnostic (Fig. 4) is the main neutron yield diagnostic on MJOLNIR. It is based on a Sandia National Labs design [14] fielded on Z Machine and was calibrated at Sandia's Ion Beam Laboratory (IBL). The calibration at IBL was specifically set up to mimic the MJOLNIR scattering environment and anticipated average neutron energy, as determined by PIC simulations, 2.8 MeV at 50° from the z-axis. Yields reported in this paper are from the Be detector, positioned at $45\text{--}50^\circ$ from the axis. The PIC simulations predict that this range of positions is approximately where the local neutron flux is equal to the 4π -averaged flux.

The Be detector was positioned between 1.33 and 1.65 m from the pinch for the majority of the shots reported here. The distance was periodically changed to accommodate other objects in the room. For one series of shots, to detector was fielded at 2.63 m to confirm the $1/r^2$ dependence when compared to a stationary cross-calibrated neutron detector, indicating that scattered neutrons did not significantly contribute to yield measurement. In all yields reported here, the distance from pinch to detector was accounted for.

The Be detector has two different photomultiplier tubes (PMTs) which independently look at the same activation

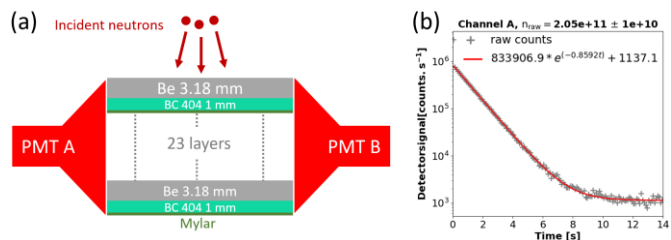


Fig. 4. (a) Be neutron activation detector schematic and (b) example single channel data from Be detector and fit.

region. Time-fits to the events observed on each PMT produces two yield measurements which are within 2% of one another.

The MJOLNIR neutron camera (Fig. 5) is similar to the fiber-coupled neutron camera used on the NIF neutron imaging diagnostic [15]. It consists of two EMI enclosures connected by a fiber-optic bundle. The first enclosure contains a BCF-99-55 [16] scintillating-plastic fiber array (Fig. 6a) made by Saint Gobain, with a 7.6 cm×7.6 cm face, and 5 cm thickness. Each fiber is 250 μm in diameter. Because the fibers confine the light produced by neutron interactions occurring along a fiber, this bundle can be thicker than a traditional scintillating screen for increased detector efficiency without causing significant spatial blur in the neutron image.

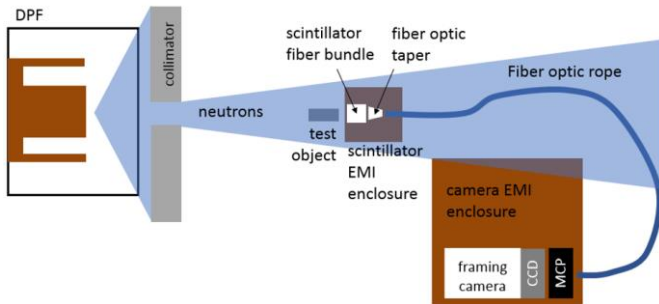


Fig. 5. MJOLNIR neutron camera set-up.

BCF-99-55 is a custom formulation which is similar to BCF-12. It emits ~8000 photons per MeV of deposited energy, at a peak wavelength of 425 nm, and a decay time of 3.2 ns. Energy deposition occurs within ~200 μm of the neutron’s location prior to interaction and average energy deposited per interacting neutron is 2.97×10^{-15} Joules. A neutron passing through 5 cm of BCF-99-55 has a ~30% chance of inducing a proton recoil event.

The fiber bundle array is optically coupled to a fiber-optic taper which is connected to a fiber optic rope running between the first and second EMI enclosures. The second enclosure, which is blocked from direct line of sight by a collimator, contains a microchannel plate (MCP) coupled to a CCD framing camera. The MCP provides time-gating for the neutron images of ~50 ns. During the 3-tower campaign, the trigger for the neutron camera time gate was derived from the master trigger that fired the DPF. A delay was included to synchronize

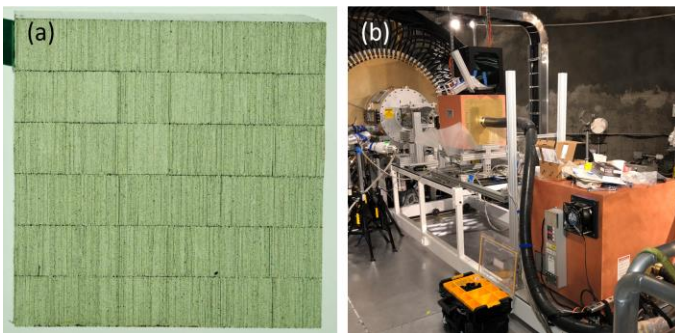


Fig. 6. (a) Front face of scintillator fiber array. The array was fabricated by making a ribbon of parallel fibers. These ribbons were overlaid to make square prisms. Finally, prisms were stacked into the final assembly shown in the image. The vertical striations are an artifact of the ribbon assembly, and the horizontal striations are an artifact of the prism assembly. (b) MJOLNIR neutron imager contained in two EMI enclosures, connected by a fiber-optic bundle. The smaller EMI enclosure contains the scintillator and fiber bundle, while the larger one, sitting in the shadow of the collimator, contains the MCP and CCD camera.

the camera with the expected neutron arrival time, which can have a 10+ ns jitter for a given set of operating parameters. Fig. 6b depicts the camera layout with respect to the DPF head.

The collimator used for the neutron image reported here had a central tungsten cylinder 10 cm thick with inner diameter of 3.5 cm and outer diameter of 10 cm. The pinch neutrons have a direct line of sight to the scintillator front face through the hole in the tungsten collimator. Additional blocks of 5.1-cm-thick polyethylene and 10.2-cm-thick lead surrounded the tungsten collimator, covering a larger solid angle, including the camera box. Additionally, 2.5 cm of borated polyethylene was placed in the line of sight from the neutrons to the camera box.

We use photodiode detectors, or “optical light gates” (Fig. 7) to measure the timing of the plasma sheath as it sweeps past a fixed location on the anode. The optical emission from the sheath is collected using a collimator, apertured to ~1 mm diameter, and transported via fiber to a biased silicon photodetector. A sharp rising edge on each light gate signal pinpoints the arrival time of the sheath at a given anode location. From these measurements we can calculate average speed between these anode locations during the run-down.

The MJOLNIR main Rogowski coil (Fig. 8) is a flat printed circuit board Rogowski that fits in a machined groove between the transmission plate and main DPF electrodes. The Rogowski diagnostic has been frequency analyzed using a network analyzer and the raw signal is frequency-corrected and then integrated to produce a current trace.

C. Simulations

MJOLNIR discharge simulations are run in the particle-in-cell code Chicago [17], typically in a fluid mode for the run-down, migrated to a fully kinetic particles description, such as in Ref. [1], or a kinetic-ions/fluid-electrons description before pinch. Cell dimensions are smaller close to the pinch location and larger farther away, typically in the range of 25 to 300 μm. The time step is adaptive based on the cyclotron frequency and typically in the range of 25–100 fs during the pinch. A D-D fusion package [18] is used to calculate yields from ion interactions. A circuit driver [19] is used to handle the boundary conditions between anode and cathode based on lumped circuit description of the drive, and includes finite cable effects. The implicit particle advance uses the direct implicit scheme [20] and collisions are included with a binary method [21, 22].

The simulations are benchmarked to neutron yield diagnostics, nToF’s at various distances, current traces, and voltage probes. A synthetic visible light diagnostic is compared

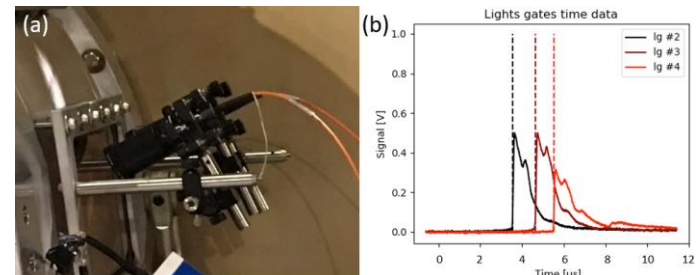


Fig. 7. (a) MJOLNIR optical light gates looking through a window in the vacuum chamber and (b) example light gate data from 3 different light gate channels. Dashed lines show arrival time of sheath from rising edge of light gate signal.

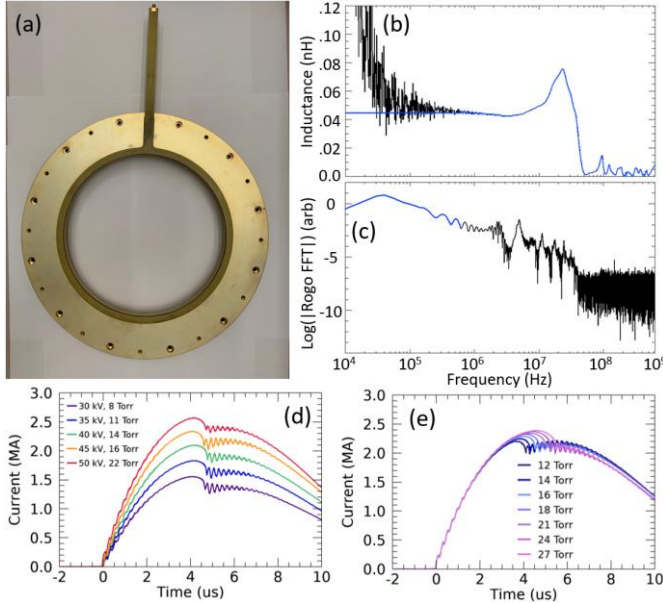


Fig. 8. (a) MJOLNIR printed circuit board Rogowski coil; (b) frequency-dependent Rogowski response as determined by network analyzer (black) and actual frequency corrections used to correct data (blue) which are flattened at low frequencies where the network analyzer has low sensitivity; (c) fast Fourier transform of Rogowski trace on a pinching MJOLNIR shot; (d) five example frequency-corrected current traces across a scaling of voltages and pressures designed to pinch at the same time. The corresponding yields are 4.1×10^{10} , 8.6×10^{10} , 1.2×10^{11} , 1.5×10^{11} , 2.1×10^{11} , and (e) frequency-corrected current traces for multiple gas fill pressures at 90 kV on anode A30-0.9-A.

to framing camera images to benchmark timing and plasma sheath shape (Fig. 9). Future diagnostics in progress, such as an interferometer, B-dots, and Faraday rotation diagnostic will provide further constraints on the model.

In addition to high-fidelity models, our team runs a variety of reduced-order models including a snowplow model [23] which is used to predict pinch timing based on a lumped circuit driver, gas fill pressure, and charging voltage. The snowplow model uses a circuit to drive 3 flat pistons which accumulate mass as the gas is swept up. A multiplier on the cross-section-averaged $J \times B$ force, unique to each anode shape, is used to achieve correct pinch timing. This multiplier is needed because in the actual device the leading edge of the sheath travels faster than the trailing edge due to the higher magnetic field at the anode. The multiplier is determined by matching timing

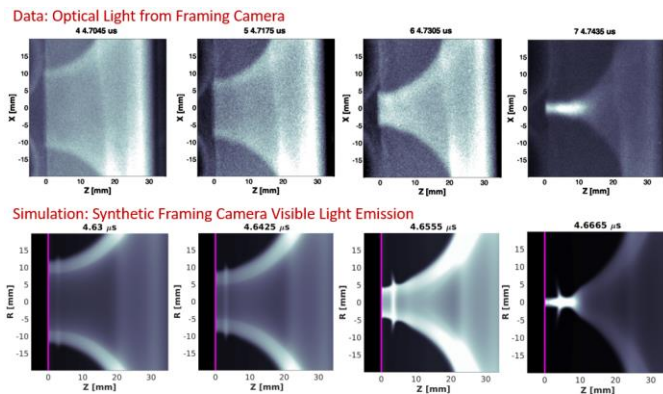


Fig. 9. Data from the optical light framing camera (top row) shows reasonable agreement with the modeled plasma sheath shape (bottom row) and timing agreement to about 1.5% under the assumption of a static gas fill/no impurities, but the modeled plasma sheath does exhibit more instabilities/ perturbations.

between the snowplow model and an MHD model for the same anode. Each anode is associated with a single multiplier that reproduces timing at multiple pressures and voltages. The snowplow model can also predict modifications to the current trace due to current restrikes which reduce gun inductance at an arbitrary time.

IV. RESULTS AND DISCUSSION

A. 1-MJ Configuration Neutron Yields and Anode Evolution

MJOLNIR was operated in the 1-MJ configuration from August 2018 to January 2020, with 436 total high-voltage plasma shots taken. The first shot to produce yield, at 60 kV erected voltage, had a measured yield of 3.1×10^{10} . The initial anodes used on MJOLNIR, had a 4.3 cm implosion radius, the radius at which the taper stops. In the MJOLNIR anodes, the taper stops at the lip surrounding the predrilled hole in the anode, typically about 0.5 cm greater than the hollow radius. These anodes were not able to scale effectively to higher yields at higher currents.

After switching to an anode with a 1.4 cm implosion radius, MJOLNIR was commissioned to full voltage with neutron yield scaling accordingly, eventually reaching up to 3.8×10^{11} . The evolution of the anode taper angle and hollow radius, based on guidance from the modeling, is discussed in section IV.D. Fig. 10 shows all yields with three towers charged, excluding warm-up shots and pre-fires, during the progression of different anodes. A warm-up shot is defined as a shot taken when yields on a particular operating day have not yet reached 1×10^{10} . Only the A30-0.9-A anode was demonstrated to reliably scale in yield with increased voltage up to maximum voltage. Shots were taken in a range of gas fill equivalent pressures from 4 to 30 torr, with the best yields in the 4–16 torr range.

Some lower performance was observed towards the end of the three-tower campaign when the MJOLNIR bank was pre-firing because of switching gas system problems that have since been resolved. For the last 37 shots of the three-tower campaign, the full six pressurized Marx towers had been attached to MJOLNIR but only three towers were charged on plasma shots.

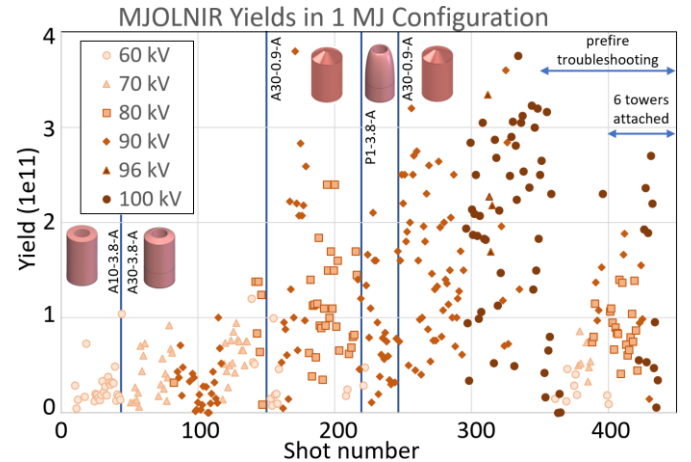


Fig. 10. Evolution of yields with three towers charged (max 1 MJ). The only anode effectively able to take advantage of the full voltage is the A30-0.9-A. Starting around shot 350, the MJOLNIR bank had frequent pre-fires due to issues in the gas switching system that eventually were resolved. For the last 37 shots shown here, the pulsed power upgrade was completed, so six pressurized Marx towers were attached, but only three were being charged on plasma shots.

B. First Neutron Radiographs

We obtained a neutron radiograph of three static test objects: a polyethylene block, a polyethylene cylinder, and a tungsten cylinder with a tapered hollow (Fig. 11). This radiograph was obtained by combining the signal from five shots taken at full voltage, 100 kV. The total yield from those five shots was 1.1×10^{12} , and the distance from the pinch to the scintillator was 2.6 m. The approximate neutron flux at the detector was 1.3×10^6 n/cm² when summed over all shots, under an assumption that neutron emission was isotropic. Likely the flux was enhanced in the forward direction but we do not at this time have a quantitative characterization of anisotropy. Before shots were combined, an imaging algorithm was used to remove artifacts caused by neutrons penetrating the camera box and hitting the CCD directly

To obtain neutron radiographs, the MJOLNIR team had to build confidence that the MCP was gated to coincide with arrival time of light from neutrons incident on the scintillator. This was done using an nToF diagnostic, with a plastic scintillator detector that was placed next to the scintillator fiber bundle, at the same distance from the pinch. The nToF diagnostic was used to establish arrival time of x-ray pulse emitted by the DPF, and the arrival time of the neutron pulse emitted by the DPF. A second nToF diagnostic that was farther away was also used to establish x-ray pulse timing, accounting for the gamma ray travel time to the detector. The second detector was also used to confirm that the travel times of the first and second peaks were consistent with the expected travel time of x-rays and neutrons respectively. The time gate on the MCP was then moved around in time, in small increments, to confirm the beginning and end of each pulse. Another confirmation of timing was made using a 6 mm thick lead plate in front of the collimator hole, which was found to have little effect on the image produced with the expected neutron timing, but greatly reduced the visibility of the image taken using the expected x-ray timing.

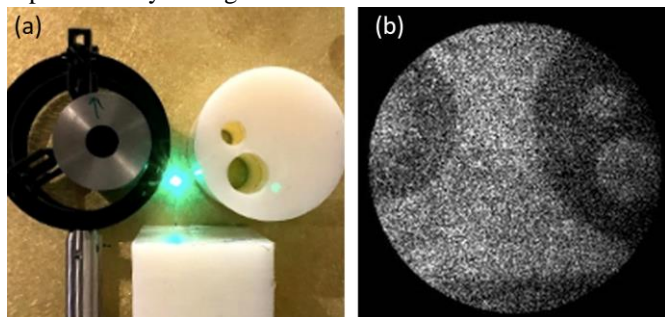


Fig. 11. (a) Test objects used for making first time-gated neutron radiograph, shown here with an alignment laser spot. (b) Early time-gated neutron radiograph compiled from 5 shots from July 18th and 19th 2019.

C. Measured Run-down and Run-in Velocities

The optical light gates provided sheath arrival time data on the first day of MJOLNIR operations, prior to neutron production. The initial configuration of light gates is shown in Fig. 12a. The light gates are used for two purposes. The first is during “conditioning” a new anode. Here data show that the sheath arrival time for subsequent shots gets faster as the day progresses, presumably as the anode is conditioned and fewer impurities are present (Fig. 12b).

Secondly, when the sheath velocity has stabilized, indicating the lack of major impurities, these speeds are used to look for trends and to benchmark the MHD and snowplow models at various fill gas pressures and voltages (Fig. 12c and 12d). Run-down speeds generally scale, as expected, inversely proportional to the square root of fill gas pressure, as well as proportional to voltage.

Once we have established pinching conditions after a vacuum break, there appears to be no correlation between yield and run-down velocity for a fixed fill pressure and charging voltage.

We have at times configured light gates at equivalent z locations on opposite sides of the vacuum chamber to investigate whether the plasma sheath is running down symmetrically. We find that any asymmetric shot had a poor yield performance but some shots had poor yields without exhibiting asymmetry.

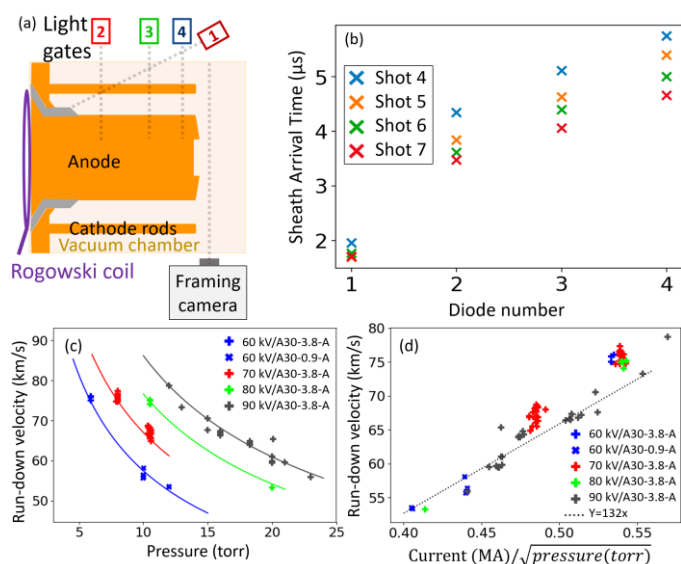


Fig. 12. (a) Light gate configuration for the first day of MJOLNIR operations, and standard location for framing camera and Rogowski coil. (b) Sheath arrival time inferred from light gates on the first day of MJOLNIR operation, demonstrating the plasma sheath was faster with each subsequent shot, presumably as the electrodes were cleaned by the plasma discharge and the density of impurities decreased. This first set of data was taken prior to MJOLNIR producing any neutron yields. (c) Run-down velocity, as inferred from optical light gate sheath arrival time, for nominal-performance neutron-producing shots at different pressures and voltages. Individual data points are shown as well as curves inversely proportional to square root of pressure. Most data shown is from anode A30-3.8-A with a few 60 kV shots shown for A30-0.9-A. (d) Run-down velocity for a variety of charging voltages and pressures, as a function of peak current divided by square-root density.

We inferred run-in speeds from optical light framing camera images. We used an edge-finding algorithm to track the plasma sheath locations (Fig. 13a) on variously timed frames, distilled the “edge” location of the sheath into a single radial location, and used timing between frames to estimate run-in speeds (Fig. 13b). We found that measured run-in speeds on different shots were similar within error bars when voltage and pressure combinations designed to preserve run-in speeds were used (Fig. 13c). Although data are limited, it appears that poor-yield shots exhibit slower run-in speeds than nominal yield shots (Fig. 13d).

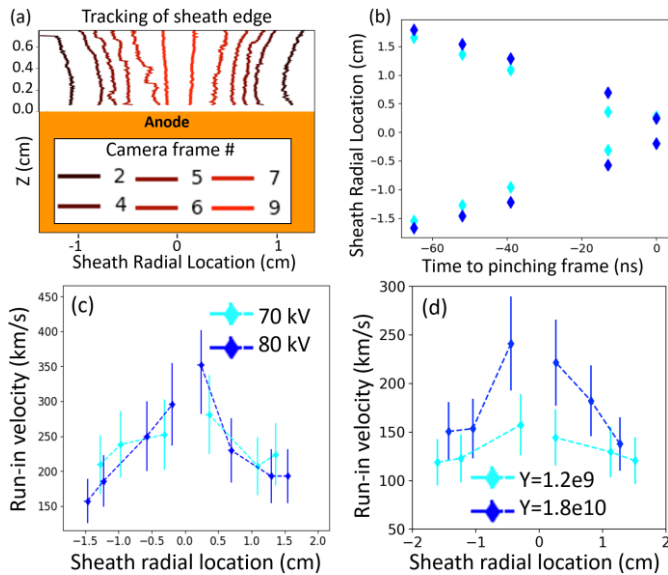


Fig. 13. (a) An edge-tracking algorithm is used to identify the leading edge of the sheath’s visible emission from camera frames. (b) The edge location is transformed into a single number representing the sheath’s leading position. (c) The positions and inter-frame times are used to produce sheath velocity as a function of location. In this case, 60 kV/6 torr and 80 kV/10.5 torr shots with pressure adjusted to preserve timing exhibited similar run-in speeds within error bars (d) This analysis shows that poor performing (low-yield) shots exhibit a slower run-in velocity, possibly attributable to current restrikes.

Optical light gate and framing camera data are not available on every shot nor every shot day due to copper coating on the chamber windows from successive discharges.

D. Likely Presence of Restrikes from Current Traces

The snowplow model has been used to interpret the dip in MJOLNIR experimental current traces at pinch time. Experimental current traces do not match snowplow simulated current traces without the introduction of a “current restrike,” introduced in the model in the form of a reduction in gun inductance at a particular time and magnitude. MJOLNIR experimental current traces are matched to simulated current traces by variation of the timing and magnitude of the restrike current.

Experimentally measured current traces from poor-yield shots match modeled current traces in which a reduction in load inductance (restrike) was introduced earlier in time, relative to higher-yield shots (Fig. 14a), indicating that current is being diverted away from the pinch region early enough to affect the neutron yield. Experimental current traces that show a deeper current dip, which in turn are correlated with higher yield [24], are consistent with modeled current traces in which the restrike happens later in time (late in the pinch or post-pinch), as compared to restrikes that happen earlier, during the implosion or early pinch. The correlation between current dip and neutron yield for MJOLNIR shots is shown in Fig. 14b.

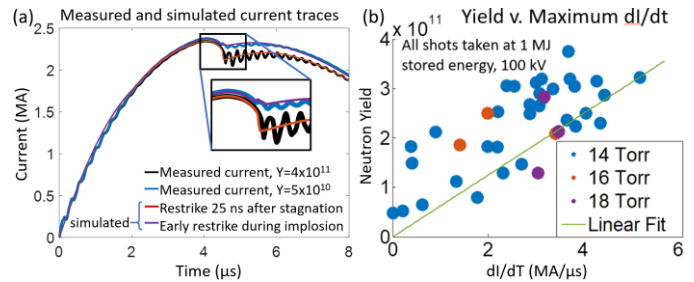


Fig. 14. (a) Measured current traces for high yield shots exhibit a deeper current dip during the pinch than do low yield shots, consistent with the delay of restrikes to the end of the pinch phase. Simulated current traces from a simple circuit/snow-plow model are matched to experimental traces by varying the timing and severity of restrikes. Simulated current traces do not include oscillations due to cable reflections. (b) Data showing relationship between yield and maximum dl/dt from Rogowski coil measurement. A bigger current dip is correlated to a larger yield. This measurement is less than ideal because the maximum dl/dt could be influenced by the timing of voltage oscillations due to cable reflections.

E. Anode Shape Optimization through Simulations

Initial simulations before the building of MJOLNIR explored anode-base radii from 5–15 cm. A radius of 7.6 cm was chosen for the expected maximum current at 1 MJ stored energy, as a reasonable tradeoff allowing for enough magnetic pressure during liftoff but keeping the length and weight of the anode manageable. Since DPFs are primarily beam-target-driven systems, simulations were performed with a focus on optimizing the target parameters for high yield.

A general issue observed in simulation for the larger radius anodes necessitated by MA-class DPFs is that the assembled target is colder by approximately $1/R_{\text{imp}}^2$. R_{imp} is the implosion radius, which sets the amount of gas that gets swept into the pinch region [25, 26] and is equal to the anode radius for a conventional flat-ended anode. As the static fill pressure of the device increases, the assembled areal density of the target increases, which increases the maximum potential yield of the device for a fixed beam energy and quantity. However, as pressure increases, plasma temperature decreases proportionally, and eventually the increased ion stopping power of the assembled target overwhelms the effect of the increased areal density.

We found that the anode radius, which partially sets the timing of the device, could be decoupled from the implosion radius using a taper at the anode tip. The taper serves to push mass axially as it is swept up, and the amount of mass that eventually resides in the pinch region is mostly set by the radius at which the taper ends. Thus, R_{imp} becomes the radius at which the taper ends, rather than the outer radius of the anode.

Anode tapering is used in the simulations to maintain plasma temperature while increasing target density. Simulations predict that decreasing the implosion radius from 4.3 cm to 1.4 cm substantially increases plasma temperature, allowing for higher fill pressures and higher yields (Fig. 15).

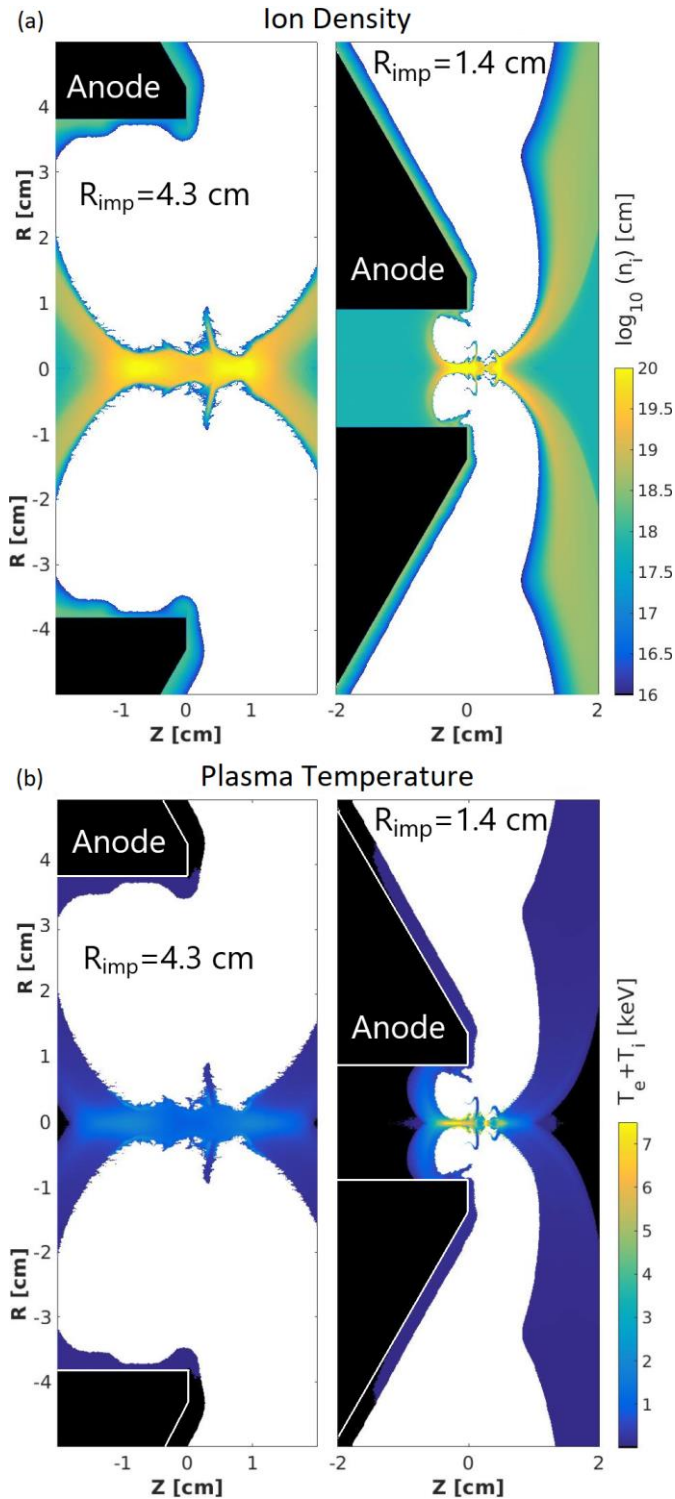


Fig. 15. (a) Simulated density during pinch for R_{imp} of 4.3 cm (hollow radius 3.8 cm) and R_{imp} of 1.4 cm (hollow radius 0.9 cm), (b) Plasma temperature for the same anodes. Simulations predict a smaller radial extent of pinch and hotter pinch for a decreased implosion radius. Simulations shown are MHD-kinetic.

A second observation in the simulations is that the assembled pinch radius decreases as the implosion radius decreases. Because the neutron source size is influenced by the size of the target that the beam interacts with, a smaller implosion radius is a promising potential pathway to decreasing the neutron source radius to improve radiographic performance. This

prediction is consistent with visible light framing camera images (Fig. 16) which show a smaller region of visible light emission for the 1.8-cm diameter hollow than for the 7.6-cm diameter hollow. Neutron spot size measurements are planned for later this year.

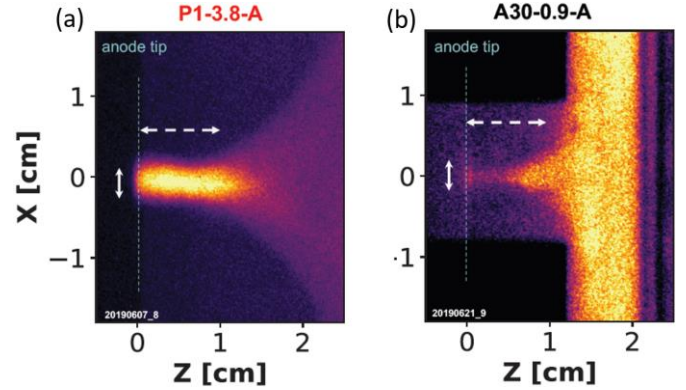


Fig. 16. Framing camera images of visible light emission for (a) anode with 3.8-inch diameter hollow and (b) 0.9-inch diameter hollow. These images suggest, but do not prove, that a smaller radius pinch (and by extension smaller neutron spot size) is achieved with a small implosion radius, consistent with predictions.

V. CONCLUSION

We commissioned the MJOLNIR DPF at maximum voltage for the initial 1 MJ stored-energy configuration, achieving yields up to 3.8×10^{11} neutrons per shot in deuterium at up to 2.5 MA peak current. Effectively using all the available voltage required modifications to the anode implosion radius, a design change guided by high-fidelity models. We commissioned and performed first measurements on several diagnostics, including a Be activation foil neutron detector, a printed circuit board Rogowski coil, optical light diodes, a visible light framing camera, and a neutron camera. We inferred run-down and run-in speeds from optical light diodes and the visible light framing camera.

Snowplow modeling of current traces matched to measured current traces suggest that shots with poor yield are losing current to a restrike early in the pinch. Additional current diagnostics, such as B-dots and Faraday rotation, are needed to confirm this result experimentally and determine the location of current loss.

A combination of MHD and PIC modeling suggested that a tapered anode can be used to control the pinch temperature, the total amount of mass going into the pinch, and the resulting pinch radius. Visible light emission suggest that the pinch radius is a function of implosion radius. Further measurements are planned to confirm experimentally whether the neutron emission radius can also be controlled by implosion radius.

Neutron camera upgrades are underway, including the use of a CCD camera with faster read-out time to reduce the registration of direct neutron hits to the CCD. It was found that the fiber optic bundle produces a low level of light even when the scintillator is not present, during the same time window as the light produced by neutrons on the scintillator. Thus the MCP has been moved to amplify the light from the scintillator

relative to the rest of the light guiding system, to improve the signal-to-background ratio relative to the initial neutron camera configuration. We also have plans to improve the trigger for the neutron camera; in the future it will be triggered off of a detector that measures the pinch x-ray signal, rather than the master trigger generator, in order to lower the jitter between the camera time gate and the neutron arrival time.

Through the addition of three more Marx towers, MJOLNIR was recently upgraded to a 2 MJ stored-energy configuration capable of up to 4 MA operation and commissioning to full voltage is underway. Data from the higher stored-energy/higher current configuration will be presented in a future work.

ACKNOWLEDGMENT

This work was performed under the auspices of the U.S. Department of Energy by Lawrence Livermore National Laboratory under Contract DE-AC52-07NA27344. The authors would like to thank the Nevada National Security Site for dispositioned Atlas capacitors, railgaps, trigger generators, and other pulsed power components that enabled this experiment. Thanks to Luis Frausto and Kurt Walters for assistance with figures. Thank you to David Fittinghoff and Dan Bower for subject matter expertise and valuable discussions on neutron imager systems. Thank you to Morry Aufderheide and Jim Hall for valuable technical discussions on neutron radiography.

REFERENCES

- [1] J.W. Mather. "Investigation of the High-Energy Acceleration Mode in the Coaxial Gun." *Physics of Fluids* 7, S28 (1964).
<https://doi.org/10.1063/1.1711086>
- [2] A. Schmidt, V. Tang, D. Welch. "Fully Kinetic Simulations of Dense Plasma Focus Z-Pinch Devices." *Physical Review Letters*, v 109 (2012): 205003.
<https://doi.org/10.1103/PhysRevLett.109.205003>
- [3] A. Schmidt, A. Link, D. Welch, V. Tang, J. Ellsworth, S. Falabella. "Comparisons of Dense Plasma Focus Kinetic Simulations with Experimental Measurements." *Physical Review E*, v89 (2014): 061101.
<http://dx.doi.org/10.1103/PhysRevE.89.061101>
- [4] A. Schmidt, A. Link, D. Welch, T. Meehan, V. Tang, C. Halvorson, M. May, E.C. Hagen. "Fully Kinetic Simulations of MegaJoule-Scale Dense Plasma Focus." *Physics of Plasmas*, v 21 (2014): 102703.
<http://dx.doi.org/10.1063/1.4897192>
- [5] S. Jiang, D. Higginson, A. Link, I. Holod, A. Schmidt. "Effect of polarity on beam and plasma target formation in a dense plasma focus." *Physics of Plasmas*, v 26 (2019): 042702.
<https://doi.org/10.1063/1.5048423>
- [6] P. Kubes, J. Kravarik, D. Klir, K. Rezac, M. Scholz, M. Paduch, I. Ivanova-Stanik, L. Karpinski, and K. Tomaszewski. "Neutron Production and Fast Deuteron Characteristics at the Plasma Focus Discharge." *AIP Conference Proceedings*. 1088, 207 (2009).
<https://doi.org/10.1063/1.3079730>
- [7] W. Kies. "Power Limits for Dynamic Pinch Discharges." *Plasma Physics and Controlled Fusion*, 28(11): p. 1645-1657 (1986).
<https://doi.org/10.1088/0741-3335/28/11/003>
- [8] H. Herold et al 1989 *Nucl. Fusion* 29 1255
- [9] N. Bennett, M. Blasco, K. Breeding, D. Constantino, A. DeYoung, V. DiPuccio, J. Friedman, B. Gall, S. Gardner, J. Gatling, E. C. Hagen, A. Luttman, B. T. Meehan, M. Misch, S. Molnar, G. Morgan, R. O'Brien, L. Robbins, R. Rundberg, N. Sipe, D. R. Welch, and V. Yuan. "Development of the dense plasma focus for short-pulse applications." *Physics of Plasmas* 24, 012702 (2017).
<https://doi.org/10.1063/1.4973227>
- [10] <https://verusresearch.net/services-and-technical-expertise/strategic-systems-engineering/>
- [11] R. A. Cooper, F. W. MacDougall, J. B. Ennis, J. C. Cochrane, W. A. Reass and W. M. Parsons, "High energy, low inductance, high current fiberglass energy storage capacitor for the Atlas Machine Marx modules," *Digest of Technical Papers. 12th IEEE International Pulsed Power Conference.* (Cat. No.99CH36358), Monterey, CA, USA, 1999, pp. 122-125 vol.1, doi: 10.1109/PPC.1999.825427.
- [12] W. M. Parsons et al., "The Atlas project-a new pulsed power facility for high energy density physics experiments," in *IEEE Transactions on Plasma Science*, vol. 25, no. 2, pp. 205-211, April 1997, doi: 10.1109/27.602492.
- [13] R. E. Reinovsky et al., "Pulsed-Power Hydrodynamics: An Application of Pulsed-Power and High Magnetic Fields to the Exploration of Material Properties and Problems in Experimental Hydrodynamics," in *IEEE Transactions on Plasma Science*, vol. 36, no. 1, pp. 112-124, Feb. 2008, doi: 10.1109/TPS.2007.914708.
- [14] Ruiz, C. L., Styron, J. D., Fehl, D. L., Hahn, K. D., McWatters, B., Mangan, M. A., ... Knapp, P. F. (2019). Novel beryllium-scintillator, neutron-fluence detector for magnetized liner inertial fusion experiments. *Phys. Rev. Accel. Beams*, 22(4), 42901.
<https://doi.org/10.1103/PhysRevAccelBeams.22.042901>
- [15] F. E. Merrill et al., "The neutron imaging diagnostic at NIF," *Review of Scientific Instruments*, 83, 10D317 (2012).
<https://doi.org/10.1063/1.4739242>
- [16] D. Fittinghoff et al., "One-dimensional neutron imager for the Sandia Z facility," *Review of Scientific Instruments* 79, 10E530 (2008).
<https://doi.org/10.1063/1.2988819>
- [17] C. Thoma, D. R. Welch, R. E. Clark, D. V. Rose, and I. E. Golovkin, *Phys. Plasmas* 24 062707 (2017)
- [18] D.P. Higginson, A. Link, A. Schmidt. "A pairwise nuclear fusion algorithm for weighted particle-in-cell plasma simulations." *Journal of Computational Physics*, v 388 (2019); 439.
<https://doi.org/10.1016/j.jcp.2019.03.020>
- [19] D. D. Hinshelwood NRL Memorandum Report 5185, Nov. 21 1983, Naval Research Laboratory.
- [20] B. I. Cohen, A. B. Langdon, and A. Friedman, *J. Comp. Phys.* 46, 15 (1982).
- [21] K. Nanbu, "Theory of cumulative small-angle collisions in plasmas" *J. Comput. Phys.* 55, 4642 (1997)
- [22] D.P. Higginson, I. Holod, A. Link, "A Corrected Method for Coulomb Scattering in Arbitrarily Weighted Particle-in-Cell Plasma Simulations" *J. Comput. Phys.* 413, 109450 (2020).
- [23] V. Tang, M. L. Adams and B. Rusnak, "Dense Plasma Focus SZ\$-Pinches for High-Gradient Particle Acceleration," in *IEEE Transactions on Plasma Science*, vol. 38, no. 4, pp. 719-727, April 2010, doi: 10.1109/TPS.2009.2037504.
<https://doi.org/10.1109/TPS.2009.2037504>
- [24] B. Bures and M. Krishnan. "An alternative scaling model for neutron production in Z-pinch devices." *Physics of Plasmas*, v 19, 112702 (2012).
<http://dx.doi.org/10.1063/1.4764894>
- [25] J. Angus, A. Link, A. Schmidt. "One-dimensional theory and simulations of the dynamic Z-pinch." *Physics of Plasmas*, v 27 (2020); 012108.
<https://doi.org/10.1063/1.5104340>
- [26] J. Angus, A. Link, A. Schmidt. "1D kinetic study of pinch formation in a dense plasma focus: Transition from collisional to collisionless regimes." *Physics of Plasmas*, v 28 (2021); 010701.
<https://doi.org/10.1063/5.0028988>